Journal of Asian Concrete Federation
Vol. 11, No. 1, pp. 53-70, March 2025
ISSN 2465-7964/ eISSN 2465-7972
DOI http://dx.doi.org/10.18702/acf.2025.11.1.53

Technical Paper

Data–driven investigation and multi–objective optimization design of alkali–activated concrete

Chang Zhou, Hong–Yuan Guo, Jian–Guo Dai*

(Received: 06-Mar-2025; Revised: 26-Mar-2025; Accepted: 27-Mar-2025; Published online: 29-Mar-2025)

Abstract: This study employs a Bayesian-optimized XGBoost algorithm to develop machine-learning models for predicting the 28-day cubic compressive strength, porosity, and CO_2 emission of alkali-activated concrete. Utilizing a dataset of 483 samples with 13 extracted input features, the models demonstrate high predictive accuracy, evidenced by robust R^2 values and low MAE, MAPE, and RMSE metrics on both training and testing datasets. The SHAP algorithm is employed to interpret the prediction process, revealing that the mass percentage of fly ash in the precursor significantly influences compressive strength and porosity. Other critical factors include curing temperature, superplasticizer-to-precursor ratio, and alkali activator-to-precursor ratio for compressive strength, while precursor dosage and water content critically affect porosity. The study suggests optimal conditions for minimizing porosity, including precursor content below 500 kg/m³, mass percentages of fly ash in precursor and the coarse aggregate content in total aggregate less than 60%, high content of Na_2SiO_3 in alkali activators. A superplasticizer-to-precursor ratio above 3% and a water-to-precursor ratio below 25% are suggested to balance workability and porosity. In addition, a multi-objective optimization framework is developed, with the target of achieving desired compressive strength of alkali-activated concrete, as well as reduced CO_2 emission and porosity.

Keywords: Alkali-activated concrete; compressive strength, porosity, machine learning; multi-objective optimization

1. Introduction

Concrete structures, such as retaining walls, bridges, and dams, face numerous challenges due to their exposure to natural environment, like rainwater, fluctuating temperatures and alkali-aggregate reaction [1,2]. The degradation of concrete structures can be caused by water infiltration and steel rebar corrosion [3,4]. To withstand these conditions and ensure long-term durability, concrete must be designed to offer excellent durability. Existing studies have demonstrated that low porosity is a key requirement, as it minimizes the ingress of water, chlorides, and aggressive substances that can lead to corrosion and deterioration [5,6]. For example, rainwater and groundwater contain various chemicals and ions, such as sulfates, which can attack the concrete and accelerate its deterioration. Low-porosity concrete limits the movement of these harmful elements, alleviating reinforcing steel corrosion and subsequent structural degradation [7,8]. Furthermore, temperature fluctuations above and below freezing are common in natural environments. Low-porosity concrete reduces the amount of water entering and trapped within the concrete, thereby improving its resistance to freeze-thaw damage [9,10].

Alkali-activated concrete (AAC), utilizing industrial by-products like fly ash and ground granulated blast-furnace slag (GGBFS), and reducing the carbon

*Corresponding author **Jian–Guo Dai,** *Department of Architecture and Civil Engineering, City University of Hong Kong, Hong Kong, China. E–mail address: jiangdai@cityu.edu.cn*
Chang Zhou, *Department of Architecture and Civil Engineering, City University of Hong Kong, Hong Kong, China. E–mail address: chang.zhou@cityu.edu.hk*
Hong–Yuan Guo, *Department of Civil and Environmental Engineering, The Hong Kong Polytechnic University, Hong Kong, China. E–mail address: hongyuan–ra.guo@polyu.edu.hk*

dioxide emission associated with the production of Portland cement, has been confirmed to have lower porosity and better durability compared to Portland cement concrete [11]. Yang et al. [12] compared the pore structure of alkali-activated fly ash geopolymer and ordinary concrete using a micro-CT scanning device and found that alkali-activated concrete has a smaller pore size (i.e. 0.5-100 μm) than ordinary Portland cement (OPC) concrete (i.e., up to 500 μm). In addition, the number of pores and volume expansion ratio of pores of alkali-activated concrete are also less than those of ordinary OPC concrete [12]. Such a phenomenon might be attributed to the introduction of alkali ions into concrete by alkali activators, initiating chemical reactions and resulting in the formation of hydration products that fill the tiny pores within the concrete, enhancing density and durability [13]. Researchers investigated the relation between the dosage of raw materials and pore structures and found that the higher content of fly ash contributes negatively to the generation of gel which will fill the pore in AAC, thereby leading to a larger porosity [13]. When NaOH is used as an alkali activator, it speeds up the hydration process of slag, leading to the rapid formation of hydration products. This rapid hydration can cause uneven material distribution, creating a poor pore structure [14]. However, such a problem can be alleviated by using Na_2SiO_4 as the alkali activator [15]. Moreover, raising the curing temperature appropriately helps dissolve slag more effectively and accelerates the hydration, leading to the formation of a larger quantity of hydration products. Besides, the elevated temperature curing also improves the crystalline structure of these products and ensures a more uniform material dispersion, contributing to a better pore structure [16].

Alkali-activated concrete is a complex composite with the use of different types of precusors and activators [17,18]. How these constituents interact with each other and influence the porosity design has not yet been fully understood. Developing accurate and reliable models for predicting the porosity of alkali-activated concrete remains as a significant challenge. As a result, there is a lack of optimization methods and guiding principles specifically aimed at designing the material porosity of AAC, hindering the determination of the optimal mix proportions and preparation techniques.

Machine learning (ML) methods have been extensively leveraged to solve complex problems in construction materials and structures, such as mechanical property prediction, capacity analysis, and multi-objective optimization [19,20]. Specifically, various ML algorithms have been explored to predict the compressive strength of AAC, like Support Vector Machine [21], Random Forest [22], Backpropagation Neural Network [23], and Adaptive Neuro-fuzzy Interface System [24]. Besides, to achieve an optimal mixture scheme for AAC that features higher strength, lower CO_2 emissions, and reduced energy consumption, Yang et al. [20] employed three standardized evaluation indexes and adopted the Gray-TOPSIS model to estimate the influence degree of each factor, and suggested optimal mixtures for AAC. Similarly, Li et al. [25] introduced a framework for the optimal design of alkali-activated slag-fly ash geopolymer concrete based on the Particle Swarm Optimization algorithm. The proposed framework aimed to achieve an optimal balance between compressive strength, cost, and carbon emissions in geopolymer concrete production. All these studies demonstrated the great potential and practical applicability of using ML algorithms for material design.

It is noteworthy that several main challenges have been identified by existing literature: (1) None of the reported ML models have accounted for the porosity of AAC, which is a critical index for the evaluation of concrete for structural applications. (2) The importance of various components in AAC on porosity is yet to be analyzed to provide design suggestions. (3) A multi-objective optimization framework for AAC design that considers porosity has not yet been developed. The present study aims to address the above knowledge gaps from the following three aspects: (1) training and testing ML models for predicting porosity, compressive strength, and CO_2 emission of AAC using existing experimental dataset; (2) ranking the importance of raw materials dosage and curing conditions, together with clarifying the positive and negative correlation of these variables with porosity of AAC; and 3) proposing a multi-objective optimization design framework for AAC application.

To achieve the above objectives, a complete

dataset that recorded the raw material content, curing condition, compressive strength, porosity, and CO_2 emission of fly ash and GGBFS-based AAC is employed for ML model training and testing. Bayesian optimization [26] and cross-validation algorithms [27] are adopted to perform hyperparameter optimization for the eXtreme Gradient Boosting Trees (XGBoost) algorithm [28]. In addition, to address the black-box nature of the ML model, the Shapley Additive exPlanations (SHAP) algorithm [29] is employed to elucidate the significance of individual features in determining the porosity and compressive strength of AAC, and provide design suggestions based on a novel parametric analysis on the entire dataset. Then, a multi-objective optimization algorithm termed Nondominated Sorting Genetic Algorithm-II (NSGA-II) [30] are adopted to perform optimal design of AAC. Finally, the codes for multi-objective optimization and pretrained XGBoost models are openly accessed to facilitate fast and optimization design of alkali-activated concrete.

2. Database description and analysis

In order to investigate the material properties of AAC, Torres et al. [31] summarized the experimental results of 1630 AAC mixes into a dataset and made it accessible to the public. The dataset meticulously documented 140 input features, which covered details of raw material content, curing conditions, and 109 output features of AAC. These output features encompassed various material properties such as compressive and tensile strength at different ages, porosity, water permeability, slump, and CO_2 emission. Given the primary objective of this article to develop prediction models for the compressive strength, porosity, and CO_2 emissions of AAC, a total of 483 samples is carefully selected. 13 parameters, including content of precursors (i.e., fly ash and GGBFS), coarse and fine aggregate content, content of alkali activators (Na_2SiO_3 and Na_2OH) and their composition, superplasticizer and total water amounts in AAC, curing temperature and curing time before demolding, are carefully chosen. Besides, a feature extraction process is conducted to explore the impact of raw material ratios on the properties of AAC [32]. In this process, the content of the precursor is considered as a unit, and new variables are created by calculating the ratios of aggregate, alkali activator, superplasticizer, and water usage to the precursor content. Hence, 13 new variables are employed as the input features of ML models, i.e., precursor content (P_c), the mass percentage of fly ash in the precursor (FA/P_c), aggregate/precursor ratio (AG/P_c), the mass percentage of coarse aggregate in total aggregate (C_{AG}/AG), alkali activator/precursor ratio (AA/P_c), Na_2SiO_3/NaOH ratio (SS/SH), Na_2O/Na_2SiO_3 ratio (S_dO/SS), SiO_2/Na_2SiO_3 ratio (S_lO/SS), NaOH concentration (M_{SH}), superplasticizer/precursor ratio (S_P/P_c), total amount of water in solutions and additional added water/precursor ratio (H_2O/P_c), curing temperature (T_p) and curing time under curing temperature before demolding (T_m). Besides, three material properties are adopted as output features, i.e., 28-day cubic compressive strength (f_c), porosity, and CO_2 emission of AAC with a volume of 1 m^3. The number of samples for f_c, porosity, and CO_2 emission regression are 455, 100, and 483, respectively. The detailed values of input and output features for each ML model can also be found in Appendix A. Furthermore, a Pearson correlation coefficient analysis [33] is performed on all 13 input features using the complete dataset consisting of 483 samples. The resulting correlations are depicted in Fig. 1. The majority of features demonstrate minimal correlations with one another, suggesting that the feature selection process for the machine learning dataset is sound. However, there exists a notable correlation between

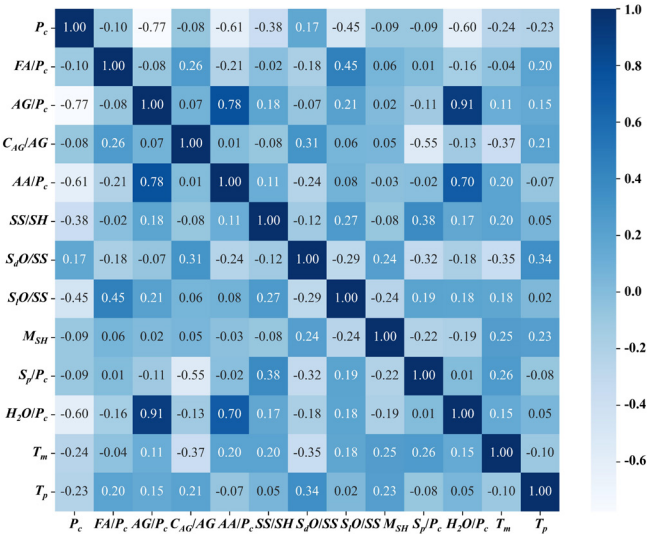

Fig. 1 Heatmap of Pearson correlation coefficient

AG/P_c and H_2O/P_c. Despite this, since both the aggregate dosage and water content are essential factors in determining the design scheme of the mixture, it is necessary to retain both parameters as input features. Besides, the data analysis statistics of 13 input features are summarized in Table 1.

Table 1 Data analysis statistics of input features

Symbols	Unit	Min	Q1	Q2	Q3	Max	Mean	STD
P_c	kg/m^3	71	360	400	450	662	402.97	106.53
FA/P_c	%	0.0	59.97	87.50	100	100	70.25	37.08
AG/P_c	/	2.09	3.89	4.47	5.18	26.52	5.11	3.40
C_{AG}/AG	%	44.68	56.10	60.46	68.04	80.51	61.37	6.98
AA/P_c	/	0.19	0.35	0.45	0.55	2.69	0.50	0.30
SS/SH	/	0.18	2.00	2.50	2.50	3.38	2.20	0.61
S_dO/SS	%	8.20	11.50	14.36	14.92	23.30	14.15	3.05
S_IO/SS	%	20.80	29.40	30.00	30.71	35.06	30.17	3.01
M_{SH}	mol/L	3	8	10	14	23	11.12	3.12
S_P/P_c	%	0.0	0.0	1.47	3.00	11.75	1.71	1.89
H_2O/P_c	%	10.67	22.96	30.04	36.45	196.79	34.23	25.55
T_m	day	0.25	1	1	1	4	1.19	0.65
T_p	℃	20	30	60	60	100	58.13	23.91

Min: Minimum; Max: Maximum; Q1, Q2, and Q3: 25th, 50th, and 75th percentiles; Mean: average value; STD: standard deviation.

3. Machine learning methods

3.1 Data normalization and splitting

Data normalization involves transforming data into a standardized scale, aiming to bring various indicators to a common dimension. The main purpose is to enable meaningful comparisons and analyses by ensuring consistent scales among different metrics. This enhances the reliability and interpretability of the results [34]. Commonly used data normalization methods include Min-Max normalization, Z-Score normalization, and Robust Scaling [35]. In this study, Max-Min normalization is utilized due to its simplicity, ability to preserve relative relationships, and retention of the original data distribution. The formula for Max-Min normalization is expressed as follows:

$$x_{ij,norm} = \frac{x_{ij} - x_{i,\min}}{x_{i,\max} - x_{i,\min}} \quad (1)$$

where x_{ij} and $x_{ij,norm}$ are the original and normalized values of the i-th feature in j-th sample, respectively; $x_{i,max}$ and $x_{i,min}$ are the maximum and minimum value of the i-th feature in all samples, respectively.

Besides, to mitigate potential ordering biases within the dataset, the normalized dataset was shuffled and divided into 80% and 20% for model training and testing, respectively.

3.2 Overview of XGBoost algorithm

The XGBoost algorithm sequentially combines a set of weak learners to form a powerful unified learner [28]. As shown in Fig. 2, it starts by training a base learner on the initial training set, and then trains additional models to correct the errors made by the previous models. This process is repeated until the desired number of base learners is achieved. Finally, these base learners are combined to generate a final prediction. In the XGBoost regressor, each tree in the ensemble is trained to rectify the errors made by the previous trees. The addition of trees continues until either the error reaches the desired level or the specified limit on the number of additions in the model constraints is reached [36,37]. The final prediction of the XGBoost algorithm is calculated as follows:

$$\hat{y}_i^{(n)} = \sum_{k=1}^{n} T_k(x_i) = y_i^{(n-1)} + T_n(x_i) \quad (2)$$

where x_i is the input features of i-th data point; Tn(x_i) is the value of i-th sample output by n-th tree; $\hat{y}i^{(n)}$ is the prediction for i-th sample made by XGBoost models.

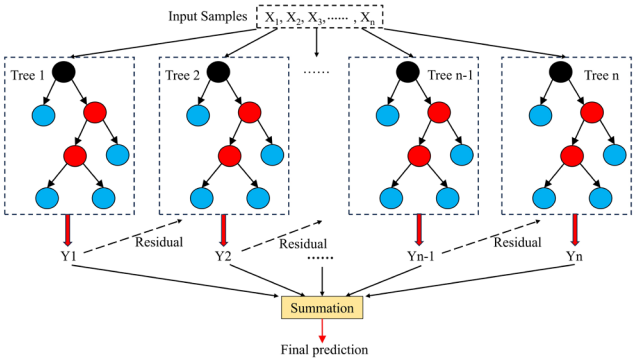

Fig. 2 Schematic diagram of XGBoost regressor

3.3 Bayesian Optimization–based hyperparameter tuning

The goal of hyperparameter optimization is to determine the best combination of parameters within the algorithm model. Several techniques are utilized for this purpose, including Grid Search, Random Search, and Bayesian Optimization [38]. Amony these methods, Bayesian optimization is known as its ability to efficiently handle the optimization of black-box functions with limited data. As illustrated in Fig. 3, by iteratively updating the surrogate model based on the observed data, Bayesian optimization intelligently explores the parameter space, focusing on promising regions and exploiting areas where the objective function is likely to be optimal. This adaptive and sequential nature of Bayesian optimization helps in effectively finding the global optimum with fewer evaluations, making it useful in scenarios where evaluating the objective function is time-consuming.

On the other hand, 10-fold Cross-validation approach was employed to assess the performance of each hyperparameter combination, and the optimal values are presented in Table 2 [27]. It involves dividing the original dataset into K equally sized subsets. Then, it iterates 10 times, where each time 9 subsets are used for training the model, and the remaining subset is used for validation. This process ensures that every subset serves as the validation set at least once. The performance of model is evaluated by averaging the results obtained from each iteration, providing a comprehensive assessment of its overall effectiveness [39].

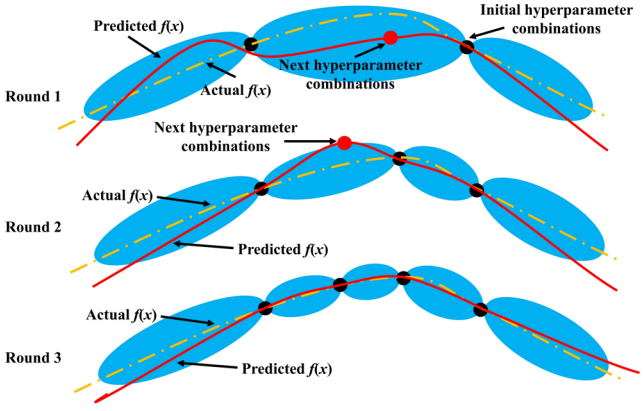

Fig. 3 Iterative process of Bayesian optimization algorithm [26]

Table 2 Optimal hyperparameter values estimated by Bayesian optimization

Hyperparameter	Values in various output features			Description
	f_c	porosity	CO_2 emission	
n_e	340	358	402	Number of estimators
l_r	0.189	0.439	0.173	Learning rate
d_{max}	7	6	7	Maximum depth of each tree
α	1	1	1	L1 regularization term coefficient
λ	1	1	0	L2 regularization term coefficient
γ0	0.794	1	1	Minimum loss reduction required to make a further partition on a leaf node
Subsample	0.733	0.482	0.780	The fraction of training samples to be chosen for each tree training
Objective	MSE	MSE	MSE	Objective function that defines specific goal that the model seeks to achieve

3.4 Performance of XGBoost models

To evaluate the performance of three XGBoost models in terms of their prediction on compressive strength, porosity and CO_2 emission of AAC, four statistical metrics are employed: mean absolute error (MAE), root mean square error (RMSE), mean absolute percentage error (MAPE), and coefficient of determination (R^2). Explanation and computational formula of these evaluation metrics can be found in our previous research [40]. For MAE, RMSE, and MAPE, lower values indicate better accuracy, with values approaching zero reflecting perfect accuracy. On the other hand, R^2 is considered optimal when it reaches a value of one, indicating an excellent fit of the model to the data.

Fig. 4 and Fig. 5 present the performance of XGBoost models on their training and testing datasets, respectively. As depicted in these figures, points located at diagonal red line indicate a prefect estimation that the predicted value is identical with experimental result. It is apparent from Fig. 4 that the trained XGBoost models exhibit high precision prediction in terms of compressive strength, porosity and CO_2 emission on the training dataset, as their values of R^2 are all larger than 0.95, and the MAPE are all less than 5%. However, the assessment of ML models on the testing dataset serves as the primary criterion for determining their acceptability. As shown in Fig. 5, the value of MAE and RMSE for models for predicting compressive

strength, porosity and CO_2 emission are 3.10 MPa vs 4.74 MPa, 0.84% vs 1.24%, 4.42 kg/m^3 vs 7.79 kg/m^3, respectively. This finding meets the acceptable criteria of ML model that the value of MAE should be smaller than that of RMSE [19]. Furthermore, the R^2 values of these models are 0.86, 0.83 and 0.94, indicating that these models are good models as their R^2 values are all larger than 0.80 [19]. Besides, as illustrated in Fig. 6, the absolute errors between the predicted and actual results are small for almost all these samples in the testing dataset, which further confirms that these XGBoost models are reasonable tools for accurate predicting the compressive strength, porosity, and CO_2 emissions of AAC.

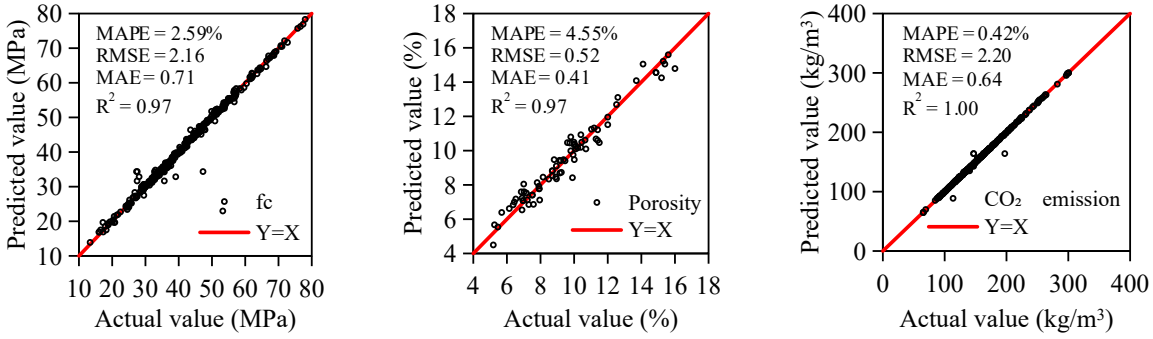

(a) f_c (b) Porosity (c) CO_2 emission

Fig. 4 Performance of ML models on training datasets

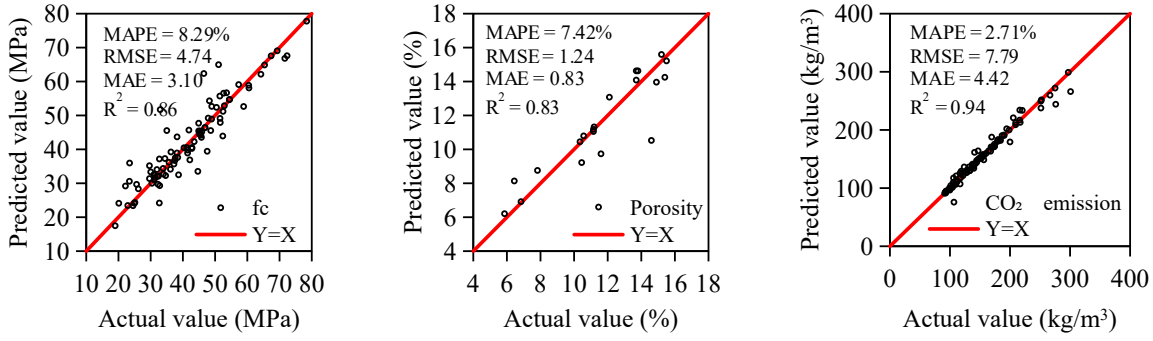

(a) f_c (b) Porosity (c) CO_2 emission

Fig. 5 Performance of ML models on testing datasets

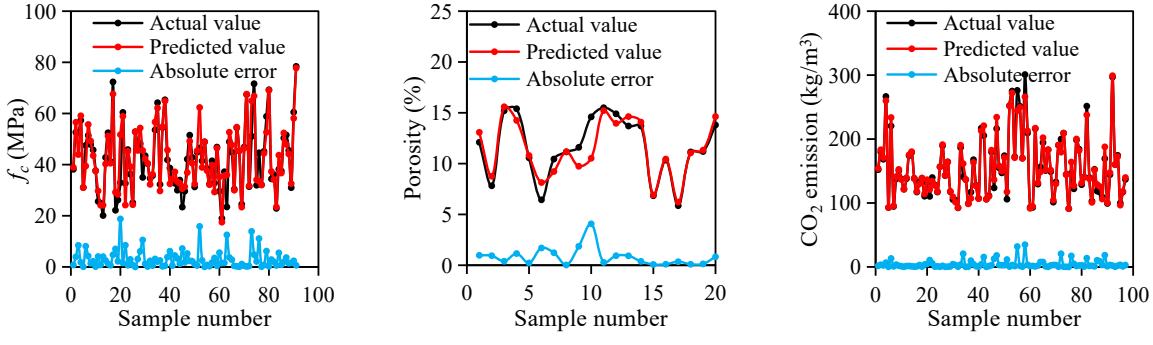

(a) f_c (b) Porosity (c) CO_2 emission

Fig. 6 Samples of experimental and predictions with error in testing dataset

4. Parametric analysis based on XGBoost models and SHAP

4.1 Overview of SHAP algorithm

Machine learning (ML) algorithms have proven to offer superior predictive accuracy in material engineering. Nevertheless, the opaque nature of their prediction processes raises concerns for engineers and designers. To tackle this issue, several post-hoc explainability techniques have been developed, such as Interpretable Mimic Learning (IML) [41], Local Interpretable Model-Agnostic Explanations (LIME) [42], and Shapley Additive Explanations (SHAP) [29]. Among these, the SHAP algorithm, which is rooted in game theory, stands out for its exceptional ability to provide both local and global explanations. Consequently, this study employs the SHAP algorithm, which represents interpretability by using Shapley values in an additive feature attribution format, as follows:

$$\hat{y} = \psi_0 + \sum_{i=1}^{n} \psi(x_i) \tag{3}$$

where ŷ is the predicted value of output features; falseis the average value of the output feature in the training dataset; n is the number of features; and false is the Shapley value of each feature on output features, which is defined as:

$$\psi(x_i) = \sum_{s \in \{x_1,\ldots,x_n\} \setminus x_i} \frac{|s|!(n-|s|-1)!}{n!} [f(s \cup \{x_i\}) - f(s)] \tag{4}$$

where $\{x_1,\ldots,x_n\}\setminus x_i$ and s represent the combination of all input features excluding the i-th feature and its subset, respectively; $|s|$ is the number of features in the subset s; $f(s)$ is the output result when considering the features in subset s; and $f(s \cup \{x_i\})$ denotes the output result when both features in subset t and i-th feature are considered.

4.2 Prediction process of XGBoost models

To illustrate the prediction process of XGBoost models, a specific sample was chosen and detailed in Table 3(a). In Fig. 7, the positive and negative contributions of each input feature on the predicted output features are represented by the red and blue columns, respectively, and the length of column indicates the absolute value of contribution provided by each feature. Table 3(a) and Fig. 7 provide insights into the selected sample. The precursor content and fly ash percentage in the sample are recorded as 350 kg/m^3 and 100%, respectively. The combination of fly ash without GGBFS has a negative impact on the 28-day cubic compressive strength of AAC. This is due to the lower chemical reactivity of fly ash compared to GGBFS when activated by alkaline solutions. The lower reactivity results in a slower and less extensive formation of the hydration product, which is responsible for the strength of alkali-activated concrete [43]. On the other hand, this combination has a positive effect on porosity, suggesting that using only fly ash as the precursor results in a higher porosity in AAC compared to using a combination of fly ash and GGBFS. The incorporation of GGBFS leads to the formation of more calcium alumino-silicate hydrate (C-A-S-H) gel, which produces additional hydration products beyond the sodium alumino-silicate hydrate (N-A-S-H) formed by fly ash [44]. This combination also has a negative impact on CO_2 emissions. This is because the CO_2 footprint associated with fly ash is significantly lower than that of GGBFS during the production and extraction process, with values of 0.004 tons and 0.052 tons, respectively [31]. Furthermore, the S_P/P_c (superplasticizer-to-precursor ratio) and H_2O/P_c (water-to-precursor ratio) are also key input features that have a negative and positive impact on the 28-day f_c and porosity, respectively. This is attributed to the absence of superplasticizer in the mixture and the reliance on water to achieve workability. As a result, the formation of hydration products occurs at a slower pace, leading to a poor pore structure and lower compressive strength [45]. The contributions of the remaining input features to the outputs of the XGBoost models can be observed in Fig.7. The SHAP algorithm combines the base value, positive and negative contributions together to generate the final predictions. As can be found in Table 3(b), the 28-day cubic compressive strength, porosity and CO_2 emission of AAC predicted by XGBoost models are 31.32 MPa, 10.45 % and 166.97 kg/m^3, respectively, resulting in relative errors of 0.42%, 0.96% and 0.49%, respectively. The subtle difference between predicted and actual results further demonstrates the effectiveness of XGBoost models.

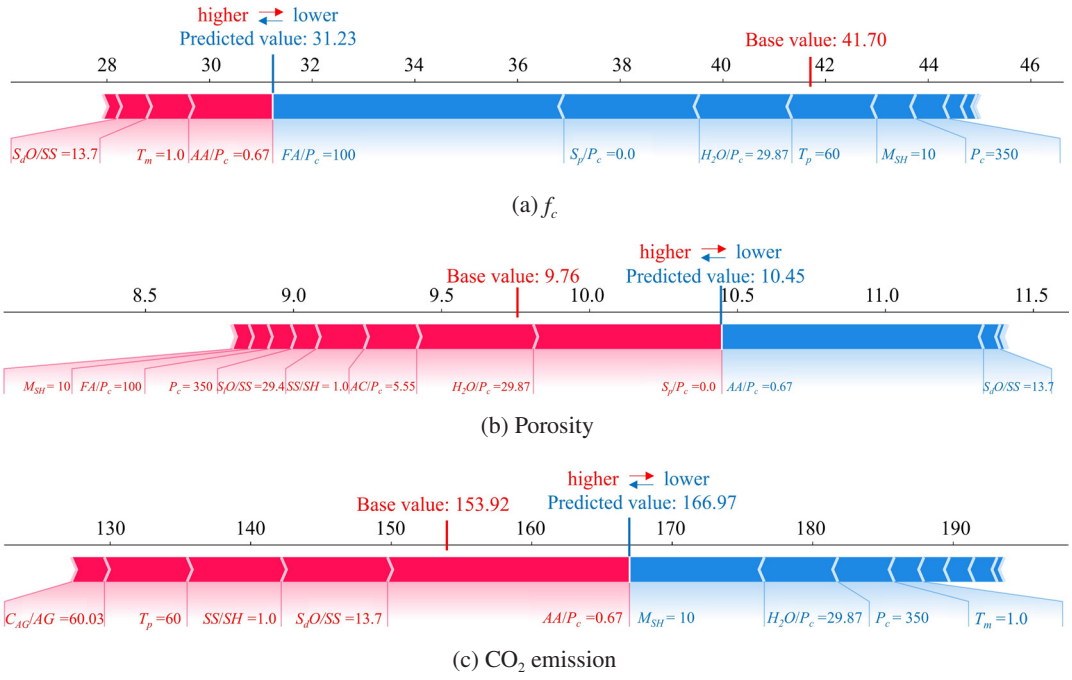

Fig. 7 Prediction process of XGBoost model

Table 3

(a) Input features of the investigated sample

P_c (kg/m^3)	FA/P_c (%)	AG/P_c (/)	C_{AG}/AG (%)	AA/P_c (/)	SS/SH (/)	S_dO/SS (%)	S_lO/SS (%)	M_{SH} (mol/L)	S_P/P_c (%)	H_2O/P_c (%)	T_m (day)	T_p (℃)
350	100	5.55	60.03	0.67	1	13.7	29.4	10.0	0	29.87	1	60

(b) Actual and predicted output features of the investigated sample

f_c (MPa)			Porosity (%)			CO_2 emission (kg/m^3)		
Actual	Predicted	Error	Actual	Predicted	Error	Actual	Predicted	Error
31.10	31.23	0.42%	10.35	10.45	0.96%	166.16	166.97	0.49%

5.3 Ranking the influence of features on compressive strength and porosity

Fig. 8 illustrates the Shapley value of each feature in each sample for XGBoost models in terms of compressive strength and porosity of AAC, and the feature positioned at the upper portion of this figure exhibits a higher influence than the feature situated at the lower section in each figure. As exhibited in Fig. 8, both the models for f_c and porosity prediction consider the mass percentage of fly ash within the precursor (FA/P_c) as the most important feature. In terms of contribution to compressive strength, curing temperature (T_p), superplasticizer-to-precursor ratio (SP/P_c) and alkali activator-to-precursor ratio (AA/P_c) are also critical features. In comparison, the influences of molar concentration of NaOH (M_{SH}), Na_2O and SiO_2 content in Na_2SiO_3 (S_dO/SS and S_lO/SS), water content (H_2O/P_c) and curing time before demolding (T_m) are less important. In contrast, the Na_2SiO_3 solution-to-NaOH solution ratio (SS/SH) shows the least important effect on the compressive strength. On the other hand, the precursor content (P_c) and water content (H_2O/P_c) also exert great impact on the porosity. In comparison, the influences of SP/P_c, AA/P_c and T_m are less significant. Conversely, the concentration and

components in alkali solutions (*SS/SH*, S_dO/SS, S_lO/SS and M_{SH}) have the least influence on the porosity of AAC.

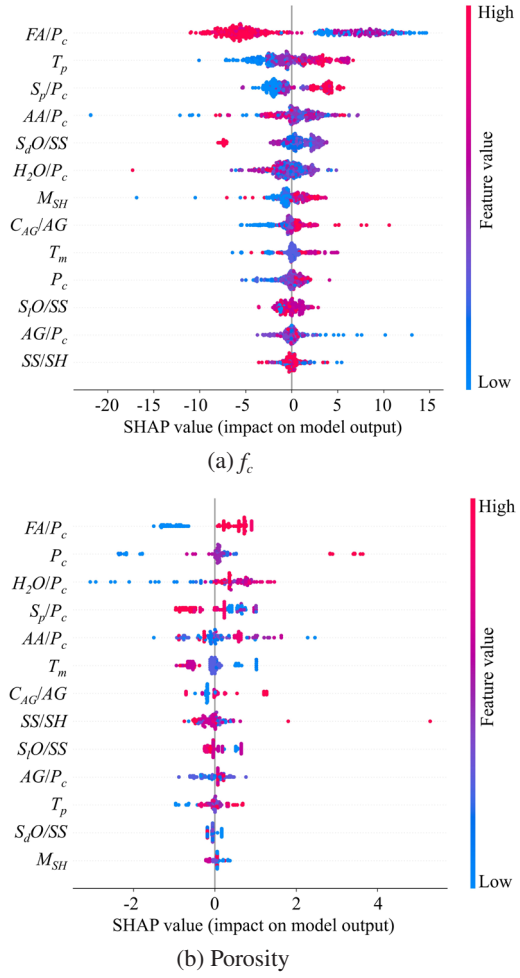

Fig. 8 Shapley value for each feature in each sample output by XGBoost model

5.4 Parametric analysis

Fig. 9 illustrates the influence of each parameter on compressive strength of AAC. It is necessary to note that each sample is represented as a point in the plot, where samples with large feature values are depicted in red. Fig. 9(a) and Fig. 9(e) show that the f_c has a positive correlation with content of precursor and alkali activator, and the upward trend will disappear while values of P_c are larger than 400 kg/m^3. This results from the fact that reactive silicon (Si) in precursor is a crucial factor in the alkali activation process, a small value of precursor content ensures the complete utilization of aluminosilicate materials during the process of alkali activation, leaving minimal unreacted particles in the mixture [46]. In contrast, an excessive amount of precursor results in complete consumption of alkali activator and the additional precursor is not involved in the reaction. Fig. 9(b) shows that the mass percentage of fly ash in precursor has a negative correlation with f_c, and a proper explanation is that compared to fly ash, GGBFS has a larger value of Si/Al ratio and a higher amount of SiO_2, which is crucial for the formation of the primary binding phase in alkali-activated materials [47]. Fig. 9(c) and Fig. 9(d) illustrates that when the proportion of coarse aggregate in the total aggregate is below 55%, the negative impact of coarse aggregate on the compressive strength of concrete decreases as its content increases. This is because coarse aggregates provide a rough surface texture and irregular shapes, which enhance interlocking between the aggregate particles and the surrounding matrix. This interlocking effect improves the load transfer mechanism, thereby resulting in an increased compressive strength [48]. Fig. 9(g) depicts the effect of Na_2O and SiO_2 content in Na_2SiO_3 solution. It is clear that these two input features will contribute positively when their values are in range of 12%-16% for S_dO/SS and 28%-34% for S_lO/SS. Fig. 9(h) indicates that the concentration of NaOH solution will contribute positively when its value reaches 10 mol/L and will contribute negatively with its value higher than 16 mol/L, which is consistent with the statistical investigation results [49]. Fig. 9(i) and Fig. 9(j) exhibit that the higher dosage of superplasticizer contribute positively to f_c, while the impact of water content is not significant. As the concentration of superplasticizer increases, the dispersion of aluminosilicate particles improves, resulting in greater water release and reduced water consumption, which in turn accelerates the reaction rate. [45]. Besides, Fig. 9(k) and Fig. 9(l) shows that the optimal curing time before demolding is about 2 days and the contribution by curing temperature will not increase if T_p is higher than 80 ℃ because the elevated curing temperatures accelerate the evaporation of water from the concrete mixture. This rapid water loss can result in shrinkage and the formation of voids, which negatively affect the compressive strength [50].

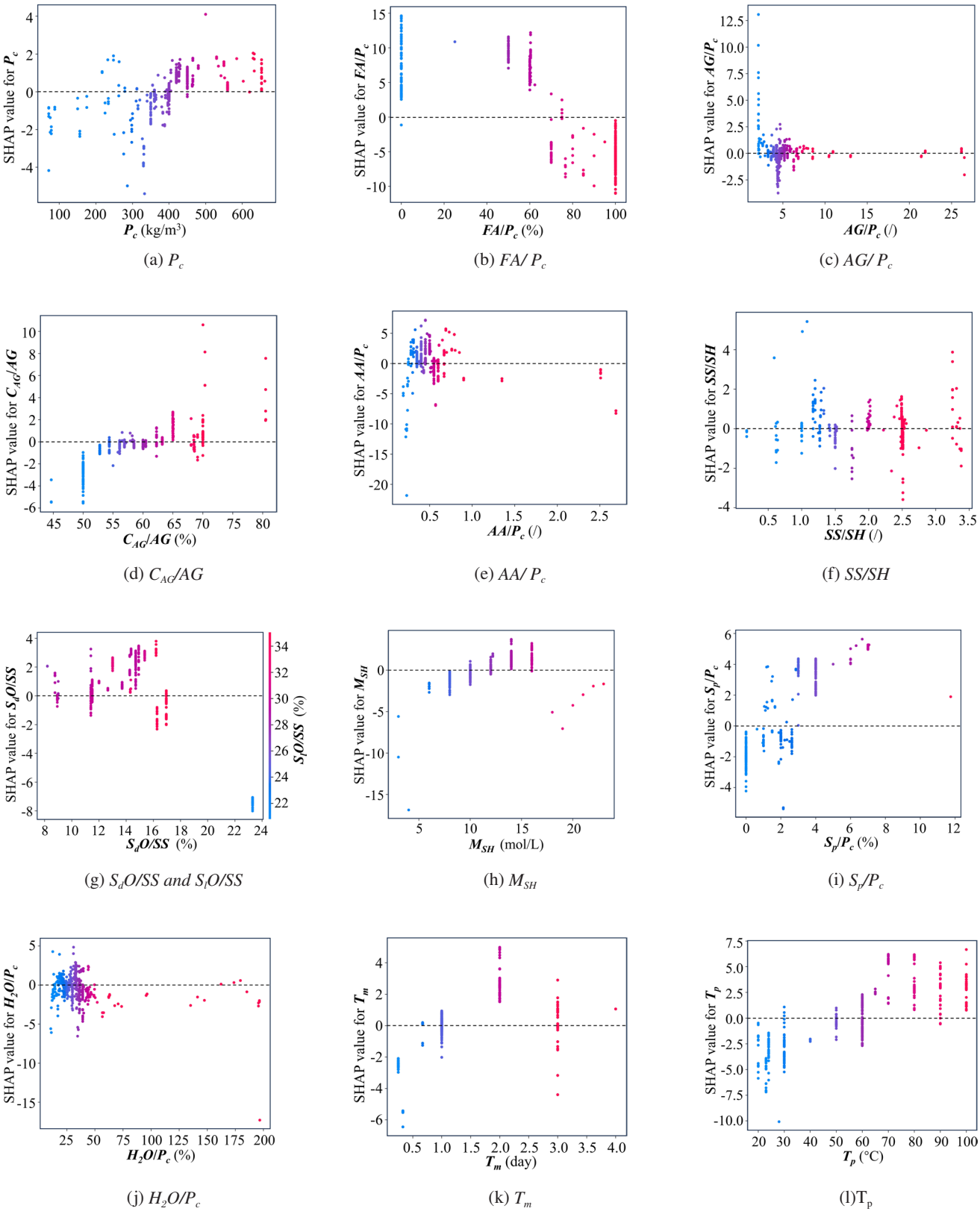

Fig. 9 SHAP value distribution of different input variables on f_c

Fig. 10 illustrates the influence of input features on the porosity of AAC. As shown in Fig. 10(a) and Fig. 10(b), the higher precursor content and fly ash percentage in precursor lead to a higher porosity. Generally, higher precursor content requires more water to achieve desired workability. This excess water can lead to higher porosity if not fully consumed in the chemical reactions, creating voids during AAC curing. Besides, fly ash is less reactive compared to GGBFS. With a higher percentage of fly ash, the slower reaction rate means that fewer binding gels are formed early on, resulting in a more porous microstructure [13]. Fig. 10(c) and Fig. 10(d) show that higher content of aggregate and the percentage of coarse aggregate in total aggregate exceeding 60% positively impact the porosity due to the increased volume of voids between the aggregate particles [51]. Fig. 10(e) and Fig. 10(f) indicate the correlation between alkali activator dosage and porosity is not clear and the porosity will be decreased if more Na_2SiO_3 is utilized in alkali activator. A reasonable explanation is that when NaOH serves as an alkaline activator, the rapid hydration reaction of slag results in accelerated formation of hydration products, leading to a rougher surface of the hydration products and uneven distribution within the matrix, thereby causing a poor pore structure. In contrast, when Na_2SiO_3 is used as an alkaline activator, the m_{Ca}/m_{Si} ratio in C-(A)-S-H decreases, leading to an increased alkaline binding capacity of C-A-S-H, which are helpful to a better pore size distribution and a denser matrix structure [13]. In addition, Fig. 10(g) shows that although the dosages of Na_2O and SiO_2 have slight influences on porosity, AAC also achieves a poor pore structure if the mass percentage of Na_2O powder is less than 12%. This is because adequate Na_2O is necessary to maintain a high pH environment, which accelerates the dissolution of silica and alumina from precursor [52]. Fig. 10(h) indicates that the alkalinity of a low concentration solution is insufficient to fully activate the precursor, which leads to incomplete dissolution, resulting in a weaker matrix with higher porosity due to unreacted particles and voids [53]. In contrast, high concentrations of NaOH solution leads to rapid setting and uneven distribution of the binding phases, creating microstructural defects and higher porosity [53]. Fig. 10(i) and Fig. 10(j) reveal that the inclusion of superplasticizer will decrease the water usage to dissolve precursor in the hydration reaction, thereby avoid the phenomenon that too much water dilute the concentration of the precursor and alkali activator, leads to poor cohesion and bonding between the particles, makes it less effective at filling the spaces between aggregates and results in a more porous structure [45]. Fig. 10(k) and Fig. 10(l) show that the longer curing time before demolding ensure the hydration reaction fully developed, thereby generating much hydration product to fill the pore in AAC. Besides, curing temperatures above 80°C result in an inferior pore structure. Excessive temperatures cause rapid moisture loss from the mixture, leading to shrinkage and the formation of voids and cracks, which increase the porosity of the AAC [50].

5. Multi–objective optimization design framework for alkali–activated concrete

5.1 Optimization problem

Based on the previous discussion, it is recommended that alkali-activated concrete should have low porosity to withstand chloride corrosion and sulphate attack. Additionally, it is crucial for the concrete to achieve the desired compressive strength. Furthermore, to promote environmental sustainability, it is important to minimize the CO_2 emissions associated with the construction material. Therefore, three objectives are taken into consideration in this study. To achieve this goal, the XGBoost models for predicting 28-day cubic compressive strength, porosity and CO_2 emission are adopted, and the optimization problem can be formulated as follows:

$$\text{objective} = f_1(x) \cup \min\left(f_2(x), f_3(x)\right) \tag{5}$$

where x is the combination of 13 input features of pretrained XGBoost models that can be utilized to obtained the dosage of each component and curing conditions of AAC; $f_1(x)$, $f_2(x)$ and $f_3(x)$ are pretrained XGBoost models for predicting compressive strength, porosity and CO_2 emission, respectively.

The constrain conditions can be expressed as follows:

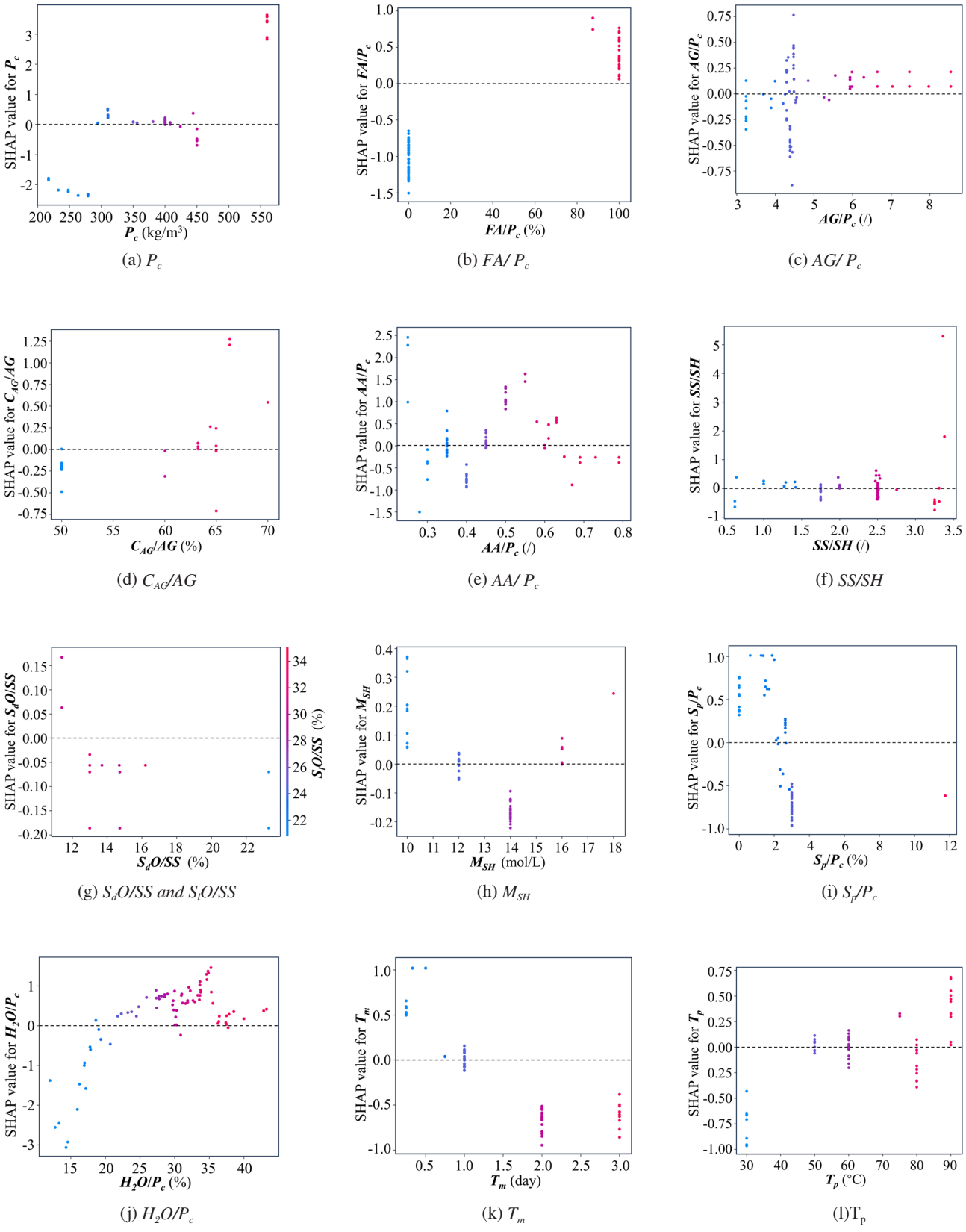

Fig. 10 SHAP value distribution of different input variables on porosity

$$f_1(x) = C \quad (6)$$

$$x = (x_1, x_2, \ldots, x_i, \ldots, x_{13}),\ x_{i,\,min} < x_i < x_{i,\,max} \quad (7)$$

where C is the required compressive strength of AAC; x_i is the i-th input feature; $x_{i,\,min}$ and $x_{i,\,max}$ are the minimum and maximum values of i-th input feature, respectively.

5.2 Optimization process

This study employes a multi-objective optimization method named Nondominated Sorting Genetic Algorithm II (NSGA-II) to construct a design framework for alkali-activated concrete. The core principle of NSGA-II is based on the concept of Pareto dominance [54]. It utilizes a non-dominated sorting mechanism to rank individuals in the population based on their dominance relationships. Individuals that are not dominated by any other individuals are considered Pareto-optimal solutions, forming the Pareto front [55].

In this study, the optimization process of NSGA-II initiates with the randomly generation of 100 samples, and then the compressive strength, porosity and CO_2 emission for each sample are obtained using the pretrained XGBoost models. Next, NSGA-II performs non-dominated sorting to determine the Pareto fronts and assign a rank to each sample [30]. The algorithm then carries out selection and crossover operations to create offspring for the next generation. It should be noted that the mutation operation is not included herein to prevent input features from exceeding their value ranges. The offspring population is combined with the parent population to form a larger population, and then the population is downsized to its original size (i.e., 100 samples) using a combination of ranking and crowding distance comparisons [56]. The above process iterates 50 times, and then the algorithm will output a set of high-quality solutions as the final Pareto front. For example, the designed cubic compressive strength of AAC is 40 MPa, as well as the porosity and CO_2 emission are considered as the optimization objectives with equal importance. Table 4 lists the minimum and maximum values of each input feature, of whose rationality can be derived from Fig. 10. Besides, to eliminate the influence of large amount of CO_2 emission caused by high curing temperature, the curing temperature is set as 20 ℃.

Table 4 Constrain conditions for input features

Input feature	P_c (kg/m^3)	FA/P_c (%)	AG/P_c (/)	C_{AG}/AG (%)	AA/P_c (/)	SS/SH (/)	S_dO/SS (%)	S_lO/SS (%)	M_{SH} (mol/L)	S_P/P_c (%)	H_2O/P_c (%)	T_m (day)	T_p (℃)
$x_{i,\,min}$	200	0	3	50	0	1	12	22	12	3	13	1	20
$x_{i,\,max}$	500	60	8	60	1	3	22	34	16	12	18	3	20

Fig. 11(a) and Fig. 11(b) illustrates the 100 design schemes in first and last generation, respectively. It is apparent that the porosity of samples in the first generation are discretely distributed between 5% and 15%, and the CO_2 emission distributed between 100 kg/m^3 to 300 kg/m^3. In comparison, the porosity and CO_2 emission of samples in the last generation are distributed between 3% and 10% and between 120 kg/m^3 and 200 kg/m^3, indicating samples that will lead to a higher porosity and CO_2 emission are eliminated in the process of iteration. Fig. 12 depicts the f_c, porosity and CO_2 emission of the best sample in each iteration. It is clear from Fig. 12(a) that the porosity of the best sample achieves an apparent decrease compared to that in the first generation. By contrast, the decrease of CO_2 emission is not significant. Besides, the compressive strength of the best sample decrease from 47 MPa to 40 MPa throughout the iteration process, shown in Fig. 12(b).

Table 5 tabulated the optimal solution for AAC mixture and curing conditions, which is plotted using red points in Fig. 11(b). With this solution, the desired compressive strength, porosity and CO_2 emission outputted by ML models are 39.52 MPa, 4.08% and 135.49 kg/m^3, respecitively.

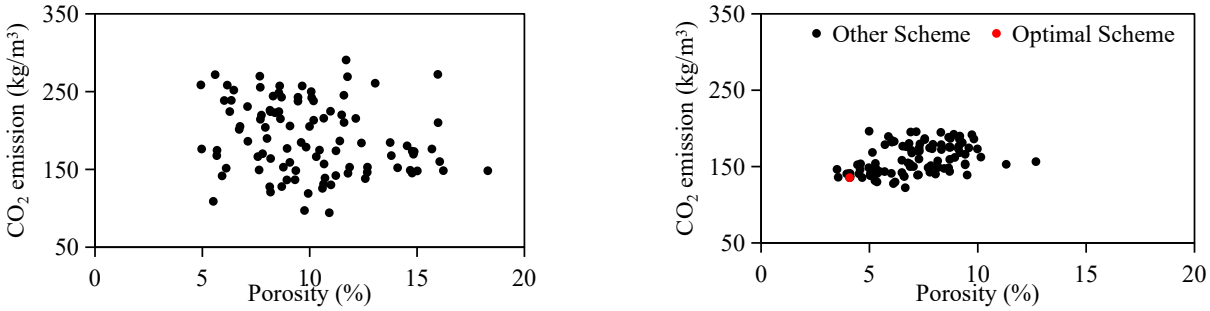

(a) 1st generation (b) 50th generation

Fig. 11 Performance of 1st and 50th generation samples

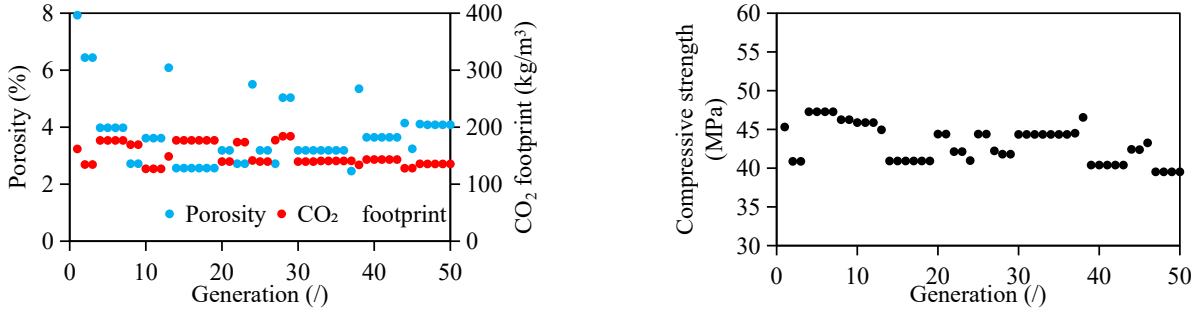

(a) Porosity and CO_2 emission (b) 28-day cubic compressive strength

Fig. 12 Performance of the best sample in each generation

Table 5 Input features value for optimal solution

P_c (kg/m^3)	FA/P_c (%)	AG/P_c (/)	C_{AG}/AG (%)	AA/P_c (/)	SS/SH (/)	S_dO/SS (%)	S_lO/SS (%)	M_{SH} (mol/L)	S_P/P_c (%)	H_2O/P_c (%)	T_m (day)	T_p (℃)
201.02	60	7.95	60	0.79	3	18.53	26.11	12.62	10.91	13.69	2.38	20

6 Conclusions

This study employs Bayesian-optimized XGBoost algorithm to regress machine learning models for predicting 28-day cubic compressive strength, porosity and CO_2 emission of alkali-activated concrete. The dataset utilized for model training and testing encompassed 483 samples and included 13 extracted input features. SHAP algorithm is utilized to elucidate the prediction process and to analyze the influence of each input feature on compressive strength and porosity. NSGA-II algorithm is adopted to perform multi-objective optimization design of alkali-activated concrete. Based on the above analysis, the following conclusions can be summarized as follows:

(1)The XGBoost models demonstrate their reliability in predicting the compressive strength, porosity, and CO_2 emission of alkali-activated concrete. The excellent predictive capabilities and generalization of these models are evident from the high R^2 value, as well as low values of MAE, MAPE, and RMSE on both training and testing datasets.

(2)The mass percentage of fly ash in the precursor is the most pivotal factor affecting the compressive strength and porosity of

AAC. In additional, the curing temperature, superplasticizer-to-precursor ratio, and alkali activator-to-precursor ratio play crucial roles in determining the compressive strength. On the other hand, the dosage of precursor and water have a significant impact on the porosity. In contrast, the Na_2SiO_3 solution-to-NaOH solution ratio, as well as the Na_2O and SiO_2 content in Na_2SiO_3, exhibit less significance compared to the other input variables.

(3) To achieve a lower porosity of AAC, it is suggested that the precursor content is less than 500 kg/m^3; mass percentages of fly ash in precursor and coarse aggregate content in total aggregate do not exceed 60%; higher content Na_2SiO_3 is utilized in alkali activator and the concentration of NaOH solution reaches 10 mol/L. Also, the values of superplasticizer-to-precursor ratio and total water-to-precursor ratio should be larger than 3% and less than 25% to balance the workability and porosity and AAC.

(4) A comprehensive multi-objective optimization design framework has been developed for alkali-activator concrete, incorporating the desired goals of achieving specific compressive strength, minimizing porosity, and reducing CO_2 emissions. An example which elaborates the optimized process is also provided to facilitate engineers understanding.

Appendix A. Supplementary data

Data for model training and testing, as well as the XGBoost models for predicting compressive strength, porosity and CO_2 emission of AAC can be found on Github: https://github.com/ChangZhouLab/Multi-objective-optimization-of-AAC.

Credit authorship contribution statement

Chang Zhou: Conceptualization, Methodology, Formal analysis, Investigation, Visualization, Validation, Writing - original draft. **Hong–Yuan Guo:** Writing - review & editing. **Jian–Guo Dai:** Resource, Project administration, Funding acquisition, Writing - review & editing.

Declaration of Competing Interest

The authors declare that they have no known competing financial interests or personal relationships that could have appeared to influence the work reported in this paper.

Acknowledgment

The authors are grateful for the financial support by NSFC/RGC Joint Research Scheme (Project No. N_CityU542/20) and the startup funding of the City University of Hong Kong "Advanced Functional Construction Materials (AFCM) for Sustainable Built Environment" (Project code 9380165).

References

[1] Jia, H.; Qiao, G.; and Han, P. (2022) "Machine learning algorithms in the environmental corrosion evaluation of reinforced concrete structures-A review," Cement and Concrete Composites, 133, pp. 104725.

[2] Uthaman, S.; and Vishwakarma, V. (2023) "Assessment of causes and consequences of concrete deterioration and its remediation," Journal of Building Engineering, 79, pp. 107790.

[3] Guo, H. Y.; Jiang, C.; Gu, X. L.; Dong, Y.; and Zhang, W. P. (2023) " Time-dependent reliability analysis of reinforced concrete beams considering marine environmental actions," Engineering Structures, 288, pp. 116252.

[4] Guo, H.; Dong, Y.; and Gu, X. (2020) "Durability assessment of reinforced concrete structures considering global warming: A performance-based engineering and experimental approach," Construction and Building Materials, 233, pp. 117251.

[5] Qu, F.; Li, W.; Dong, W.; Tam, V. W.; and Yu, T. (2021) "Durability deterioration of concrete under marine environment from material to structure: A critical review," Journal of Building Engineering, 35, pp. 102074.

[6] Huang, D.; Niu, D.; Zheng, H.; Su, L.; Luo, D.;

and Fu, Q. (2020) "Study on chloride transport performance of eco-friendly coral aggregate concrete in marine environment," Construction and Building Materials, 258, pp. 120272.

[7] Li, Q.; Ren, Z.; Su, X.; Feng, Y.; Xu, T.; Zheng, Z.; Liu, Y.; and Li, P. (2024) "Improving sulfate and chloride resistance in eco-friendly marine concrete: Alkali-activated slag system with mineral admixtures," Construction and Building Materials, 411, pp. 134333.

[8] Rasheed, Q.; Sikandar, M. A.; Khan, M. H.; Akash, K.; Nasir, H.; and Khan, B. J. (2021) "Assessment of chloride-induced reinforcement corrosion protection of modified sulfur polymer composites," Construction and Building Materials, 268, pp. 121086.

[9] González, D. C.; Mena, Á.; Mínguez, J.; and Vicente, M. A. (2021) "Influence of air-entraining agent and freeze-thaw action on pore structure in high-strength concrete by using CT-Scan technology," Cold Regions Science and Technology, 192, pp. 103397.

[10] Liu, M.; Qiao, P.; and Sun, L. (2021) "Dependence of chloride ion diffusivity on evolution of pore-structures in freeze-thawed shotcrete: Multiscale characterization and modeling," Cement and Concrete Composites, 123, pp. 104222.

[11] Lao, J.; Huang, B.; Fang, Y.; Xu, L.; Dai, J. G.; and Shah, S. P. (2023) "Strain-hardening alkali-activated fly ash/slag composites with ultra-high compressive strength and ultra-high tensile ductility," Cement and Concrete Research, 165, pp. 107075.

[12] Yang, M.; Paudel, S. R.; and Asa, E. (2020) "Comparison of pore structure in alkali activated fly ash geopolymer and ordinary concrete due to alkali-silica reaction using micro-computed tomography," Construction and Building Materials, 236, pp. 117524.

[13] Fu, Q.; Bu, M.; Zhang, Z.; Xu, W.; Yuan, Q.; and Niu, D. (2023) "Hydration characteristics and microstructure of alkali-activated slag concrete: a review," Engineering, 20, pp. 162-179.

[14] Zhang, Y.; Wan, X.; Hou, D.; Zhao, T.; and Cui, Y. (2018) "The effect of mechanical load on transport property and pore structure of alkali-activated slag concrete," Construction and Building Materials, 189, pp. 397-408.

[15] Hu, X.; Shi, C.; Liu, X.; and Zhang, Z. (2020) "Studying the effect of alkali dosage on microstructure development of alkali-activated slag pastes by electrical impedance spectroscopy (EIS)," Construction and Building Materials, 261, pp. 119982.

[16] Wei, X.; Li, D.; Ming, F.; Yang, C.; Chen, L.; and Liu, Y. (2021) "Influence of low-temperature curing on the mechanical strength, hydration process, and microstructure of alkali-activated fly ash and ground granulated blast furnace slag mortar," Construction and Building Materials, 269, pp. 121811.

[17] Lao, J.; Ma, R.; Xu, L.; Li, Y. ; Shen, Y.; Yao, J. ; Wang, Y.; Xie T.; and Huang, B. (2024) "Fly ash-dominated high-strength engineered/strain-hardening geopolymer composites (HS-EGC/SHGC): influence of alkalinity and environmental assessment," Journal of Cleaner Production, 447, pp. 141182.

[18] Qu, X.; Guo, T.; Cai, J.; Hu, Y.; Huang, B.; and Xie, T. (2025) "Characterization and analysis of electrothermal, thermoelectric, and current discharge properties of alkali-activated materials: Implications for energy conversion," Cement and Concrete Composites, 159, 105987.

[19] Khan, M.; Lao, J.; and Dai, J. G. (2022) "Comparative study of advanced computational techniques for estimating the compressive strength of UHPC," Journal of Asian Concrete Federation, 8(1), pp. 51-68.

[20] Yang, Z.; Zhan, X.; Zhu, H.; Zhang, B.; Feng, P.; Li, H.; and Kua, H. W. (2023) "Performance-based alkali-activated seawater sea-sand concrete: Mixture optimization for mechanical, environmental, and economical objectives," Construction and Building Materials, 409, pp. 134156.

[21] Peng, Y.; and Unluer, C. (2022) "Analyzing the mechanical performance of fly ash-based geopolymer concrete with different machine learning techniques," Construction and Building

Materials, 316, pp. 125785.
[22] Gomaa, E.; Han, T.; ElGawady, M.; Huang, J.; and Kumar, A. (2021) "Machine learning to predict properties of fresh and hardened alkali-activated concrete," Cement and Concrete Composites, 115, pp. 103863.
[23] Pham, T. T.; Nguyen, T. T.; Nguyen, L. N.; and Nguyen, P. V. (2020) "A neural network approach for predicting hardened property of geopolymer concrete," GEOMATE Journal, 19(74), pp. 176-184.
[24] Khan, M. A.; Zafar, A.; Farooq, F.; Javed, M. F.; Alyousef, R.; Alabduljabbar, H.; and Khan, M. I. (2021) "Geopolymer concrete compressive strength via artificial neural network, adaptive neuro fuzzy interface system, and gene expression programming with K-fold cross validation," Frontiers in Materials, 8, pp. 621163.
[25] Li, Y.; Shen, J.; Lin, H.; and Li, Y. (2023) "Optimization design for alkali-activated slag-fly ash geopolymer concrete based on artificial intelligence considering compressive strength, cost, and carbon emission," Journal of Building Engineering, 75, pp. 106929.
[26] Zhou, C.; Xie, Y.; Wang, W.; and Zheng, Y. (2023) "Machine learning driven post-impact damage state prediction for performance-based crashworthiness design of bridge piers," Engineering Structures, 292, pp. 116539.
[27] Zhou, C.; Tan, X.; Zheng, Y.; Wang, Y.; and Mahjoubi, S. (2025) "Data-driven axial bearing capacity analysis of steel tubes infilled with rubberized alkali-activated concrete," Advances in Structural Engineering, 28(1), pp. 145-158.
[28] Chen T, Guestrin C. (2016) "A scalable tree boosting system," Proceedings of the 22nd acm sigkdd international conference on knowledge discovery and data mining, New York, United States.
[29] Lundberg, S. M.; and Lee, S. I. (2017) "A unified approach to interpreting model predictions," Advances in neural information processing systems, Long Beach, CA, USA.
[30] Ma, H.; Zhang, Y.; Sun, S.; Liu, T.; and Shan, Y. (2023) "A comprehensive survey on NSGA-II for multi-objective optimization and applications," Artificial Intelligence Review, 56(12), pp. 15217-15270.
[31] Torres, B. M.; Völker, C.; and Firdous, R. (2023) "Concreting a sustainable future: A dataset of alkali-activated concrete and its properties," Data in Brief, 50, pp. 109525.
[32] Rathnayaka, M.; Karunasinghe, D.; Gunasekara, C.; Wijesundara, K.; Lokuge, W.; and Law, D. W. (2024) "Machine learning approaches to predict compressive strength of fly ash-based geopolymer concrete: A comprehensive review," Construction and Building Materials, 419, pp. 135519.
[33] Asuero, A. G.; Sayago, A.; and González, A. G. (2006) "The correlation coefficient: An overview," Critical reviews in analytical chemistry, 36(1), pp. 41-59.
[34] Singh, D.; and Singh, B. (2020) "Investigating the impact of data normalization on classification performance," Applied Soft Computing, 97, pp. 105524.
[35] Jain, A.; Nandakumar, K.; and Ross, A. (2005) "Score normalization in multimodal biometric systems," Pattern recognition, 38(12), pp. 2270-2285.
[36] Friedman, J. H. (2002) "Stochastic gradient boosting," Computational statistics and data analysis, 38(4), 367-378.
[37] Hsu, A.; Wang, X.; Tan, J.; Toh, W.; and Goyal, N. (2022) "Predicting European cities' climate mitigation performance using machine learning," Nature Communications, 13(1), pp. 7487.
[38] Wu, J.; Chen, X. Y.; Zhang, H.; Xiong, L. D.; Lei, H.; and Deng, S. H. (2019) "Hyperparameter optimization for machine learning models based on Bayesian optimization," Journal of Electronic Science and Technology, 17(1), pp. 26-40.
[39] Fushiki, T. (2011) "Estimation of prediction error by using K-fold cross-validation," Statistics and Computing, 21, pp. 137-146.
[40] Zhou, C.; Wang, W.; and Zheng, Y. (2024) "Data-driven shear capacity analysis of headed stud in steel-UHPC composite structures,"

Engineering Structures, 321, pp. 118946.
[41] Che, Z.; Purushotham, S.; Khemani, R.; and Liu, Y. (2017) "Interpretable deep models for ICU outcome prediction," AMIA annual symposium proceedings, Washington, DC, USA.
[42] Hakkoum, H.; Idri, A.; and Abnane, I. (2024) "Global and local interpretability techniques of supervised machine learning black box models for numerical medical data," Engineering Applications of Artificial Intelligence, 131, pp. 107829.
[43] Häkkinen, T. (1993) "The influence of slag content on the microstructure, permeability and mechanical properties of concrete Part 1 Microstructural studies and basic mechanical properties," Cement and Concrete Research, 23(2), pp. 407-421.
[44] Nath, P.; and Sarker, P. K. (2014) "Effect of GGBFS on setting, workability and early strength properties of fly ash geopolymer concrete cured in ambient condition," Construction and Building materials, 66, pp. 163-171.
[45] Ramujee, K.; and PothaRaju, M. (2017) "Mechanical properties of geopolymer concrete composites," Materials today: proceedings, 4(2), pp. 2937-2945.
[46] Ravikumar, D.; and Neithalath, N. (2012) "Effects of activator characteristics on the reaction product formation in slag binders activated using alkali silicate powder and NaOH," Cement and Concrete Composites, 34(7), pp. 809-818.
[47] Sun, X.; Zhao, Y.; Qiu, J.; and Xing, J. (2022) "Alkali-activated blast furnace slag for eco-friendly binders," Journal of Materials Science, pp. 1-24.
[48] Shen, W.; Wu, M.; Zhang, B.; Xu, G.; Cai, J.; Xiong, X.; and Zhao, D. (2021) "Coarse aggregate effectiveness in concrete: Quantitative models study on paste thickness, mortar thickness and compressive strength," Construction and Building Materials, 289, pp. 123171.
[49] Rai, B.; Roy, L. B.; and Rajjak, M. (2018) "A statistical investigation of different parameters influencing compressive strength of fly ash induced geopolymer concrete," Structural Concrete, 19(5), pp. 1268-1279.
[50] Zeyad, A. M.; Tayeh, B. A.; Adesina, A.; de Azevedo, A. R.; Amin, M.; Hadzima-Nyarko, M.; and Agwa, I. S. (2022) "Review on effect of steam curing on behavior of concrete," Cleaner materials, 3, pp. 100042.
[51] de Oliveira Haddad, L. D.; Neves, R. R.; de Oliveira, P. V.; dos Santos, W. J.; and de Carvalho Junior, A. N. (2020) "Influence of particle shape and size distribution on coating mortar properties," Journal of Materials Research and Technology, 9(4), pp. 9299-9314.
[52] Ji, X.; Wang, Z.; Wang, X.; Zhao, X.; Zhang, H.; and Zhang, T. (2024) "Microstructures and properties of alkali-activated slags with composite activator: effects of Na2O equivalents," Journal of Cleaner Production, 450, pp. 141754.
[53] Xie, T.; Visintin, P.; Zhao, X.; and Gravina, R. (2020) "Mix design and mechanical properties of geopolymer and alkali activated concrete: Review of the state-of-the-art and the development of a new unified approach," Construction and Building Materials, 256, pp. 119380.
[54] Voorneveld, M. (2003) "Characterization of pareto dominance," Operations Research Letters, 31(1), pp. 7-11.
[55] Huang, G.; Abou-Chakra, A.; Geoffroy, S.; and Absi, J. (2024) "Improving the mechanical and thermal performance of bio-based concrete through multi-objective optimization," Construction and Building Materials, 421, pp. 135673.
[56] Zhang, P.; Qian, Y.; and Qian, Q. (2021) "Multi-objective optimization for materials design with improved NSGA-II," Materials today communications, 28, pp. 102709.